Engineered Science
DOI: https://dx.doi.org/10.30919/es1697

# Research on Flow Simulation and Design Optimization of Large-size Fused Deposition Manufacturing Printing Nozzle

Jinyun Jiang,[1] Jiaxin Wu,[1] Chenchao Fu,[3] Zhenyu Wang,[1, 2] Haoyu Zhu[1] and Jianchen Cai[1, 2, *]

## Abstract

Fused deposition modeling (FDM) technology is widely adopted in production and typically uses 0.4 mm nozzles for precision printing, but there is little research on large-bore nozzles. Therefore, this paper designs a nozzle with a nozzle diameter (d) of 3 mm, and uses orthogonal design combined with Polyflow to systematically study the influence of nozzle structural parameters on the flow characteristics of polylactic acid (PLA) melt. Using Range Analysis Method, the significance of each parameter was clarified, and the best nozzle structure combination was obtained by optimization using Genetic Algorithm (GA). It was found that, among the structural parameters, liquefier diameter (D) has the most significant effect on the melt flow characteristics, and its increase can enhance the outlet velocity but reduce the melt viscosity; outlet length (L3) has the greatest effect on the pressure distribution, and the pressure decreases with the increase of $L_3$; and the effect of the nozzle length (L2) is relatively small. The optimized nozzle structure (D = 15 mm, $L_2$ = 23-24 mm, $L_3$ = 7 mm) achieves better overall performance. The results of this research can provide a certain theoretical basis for the design of large-bore nozzles for industrial-grade FDM equipment.

*Keywords:* Fused deposition modeling; Genetic Algorithm; Nozzle structure; Polyflow simulation; Orthogonal experiment.

Received: 03 July 2025; Revised: 14 August 2025; Accepted: 28 August 2025.
Article type: Research article.

## 1. Introduction

3D printing technology is an advanced manufacturing method based on digital modeling. It is capable of building a specific model or structure by adding material layer by layer according to a preset layering thickness and stacking path.[1,2] At present, 3D printing technology can be specifically divided into: fused deposition modeling (FDM), selective laser sintering (SLS), stereolithography (SLA), and laminated object manufacturing (LOM), *etc.*, of which FDM technology is more widely used.[3-6]

As a research hotspot for 3D printing technology, FDM technology is becoming increasingly popular and widely used in industry due to its small size, ease of use, universal operator interface, and ability to fabricate multifunctional parts.[7] With the continuous advancement of processes and materials, FDM technology has gradually matured and has also been more and more widely used in different fields, such as automotive,[8] aerospace,[9] medical,[10] architecture,[11] and art and design.[12] These industry sectors have effectively reduced production costs and improved efficiency through the application of FDM technology, for instance, in manufacturing, traditional production methods typically require expensive molds and tooling to produce small batches of parts, resulting in high upfront costs. However, by adopting FDM 3D printing technology, manufacturers can directly manufacture these parts based on digital models in layers, thereby eliminating the mold manufacturing step and reducing tooling costs.[13] The main materials commonly used in FDM technology are metals, ceramics, polymers and even living cells, among which polymers include PLA, nylon (PA) and acrylonitrile-butadiene-styrene (ABS).[14-18] Among them, PLA is a polyester polymer material, which is a natural polymer compound derived from renewable resources with good biocompatibility and biodegradation properties and is an environmentally friendly green material.[19-22]

Currently, the nozzle diameter (d) of the printing filament on the market is 0.75 mm, and FDM printers are commonly

[1] *College of Mechanical Engineering, Quzhou University, Quzhou, 324000, China*
[2] *Quzhou Resource Chemical Industry Innovation Research Institute, Quzhou, 324000, China*
[3] *College of Mechanical and Electrical Engineering, Beijing University of Chemical Technology, Beijing, 100029, China*
**Email:* cai198666@126.com (J. Cai)

equipped with 0.2-0.5 mm diameter nozzles to adapt the printing filament to achieve high-precision printing and meet most production requirements.[23] However, in the field of large industrial parts manufacturing, small-bore nozzles have inherent defects of low extrusion efficiency and slow molding speed. Studies have shown that an appropriate increase in d can significantly improve the printing efficiency, TEZEL *et al*.[24] found through systematic analysis that in the range of 0.2-1.2 mm, increasing d not only shortens the printing time, but also improves the strength of the part. However, when d is further increased to 3 mm and other industrial-grade apertures, the existing studies have obvious deficiencies: on the one hand, there is a lack of optimization studies on the runner structure for large-bore nozzles; on the other hand, the key issues of the regulation of melt rheological behavior and the control of the temperature field uniformity under high-flow conditions have not yet been systematically solved. These technical bottlenecks seriously limit the application of large-bore FDM printers in industrial scenarios such as large functional parts manufacturing. Therefore, an intensive study of the structural design and process optimization of large-bore nozzles of 3 mm and above is of great theoretical and engineering value to promote FDM technology toward industrialized production.

The nozzle of a 3D printer is the core component of the printing system. Its structural design has a great influence on the stability of filament exit and the print quality of the workpiece.[23] Presently, Computational Fluid Dynamics (CFD) simulation, orthogonal design of experiments and rheological experiments are the mainstream methods in the field of 3D printing nozzle design. Among them, CFD evaluates the design rationality by simulating the melt flow behavior (shear rate field, pressure field, and temperature field), and commonly used software includes ANSYS Polyflow, COMSOL Multiphysics, Autodesk CFD, OpenFOAM, and Siemens STAR-CCM+.[23,25] Orthogonal experimental design combined with range analysis can quantify the effect of nozzle parameters on print quality.[26] The combined application of these methods provides a complete validation system for nozzle design from theory to practice. In related research, HIKMAT *et al*.[27] used Taguchi's partial factorial design method to investigate the effects of d, extruder temperature, filler density, and extrusion speed on the tensile strength of PLA specimens, and concluded that the d, and filler density have a significant effect on the strength of PLA specimens. SINGH *et al*. [28] conducted a multi-objective optimization of FDM process based on GA which concluded that the best print manufacturing results were achieved at a printing temperature of 244.9 °C, a printing layer height of 0.2 mm and a filler pattern of serrated pattern. FISCHER *et al*.[29] increased the yield strength of 3D printed molded parts up to 75% and the elongation at break up to 70% by varying the parameters of the extrusion d and the layer height *etc*. Hutchinson *et al*.[30] investigated the strength of PLA specimens in three groups of 3D printed specimens by means of a simulation experiments, investigated the melt flow properties and the effects of feeding rate and extrusion temperature on the extruded polymer with three sets of nozzles, and concluded that the feeding rate is a key factor affecting polymer extrusion, while the symmetric design of the nozzle affects the extrusion stability.

In addition, Yu *et al*.[31] analyzed the nozzle structure by orthogonal experiment and COMSOL simulation, optimized the nozzle structure parameters for PLA and ABS materials, and concluded that the d is inversely proportional to the printing accuracy. Inside the 3D printing nozzle, the melt flow channel is usually small, and the material properties transition from the macroscopic scale to the microscopic scale inside the nozzle, and the microscopic size effect will have an impact on the stacking morphology of the material during the 3D printing process.[32] At the microscopic scale, the viscoelasticity of the printed material decreases with the decrease of the flow channel size, which in turn affects the rheological behavior of the melt.[33] Xu *et al*.[34] by constructing a microscopic viscosity mathematical model and combining it with experimental studies of microchannel molds of different diameters, found that when the shear rate is the same, the decrease of the flow channel size leads to a decrease in the viscosity of the melt, resulting in a viscosity difference. The viscosity difference decreases with the increase of shear rate, which provides theoretical and experimental references for flow simulation and nozzle design in 3D printing nozzles.

For the problem that small-bore nozzles are difficult to meet the efficient production of industrial-grade large parts, this paper designs a 3D printing nozzle structure with a d of 3 mm, and numerically simulates the flow field inside the nozzle using Polyflow, focusing on the distribution characteristics of the pressure field, temperature field, velocity field and shear rate field under different structural parameters, so as to quantify the influence of the nozzle structure on the 3D printing effect. In addition, by systematically analyzing the flow channel structure of the 3D printing nozzle and optimizing the experimental results with the Genetic Algorithm (GA), this paper finally obtains a 3D printing nozzle model with better comprehensive performance indexes. This study improves the working precision and efficiency of the nozzle with large d, which is of significance for the development of large-bore nozzle FDM printers.

## 2. Materials and methods

### 2.1 3D printer

Fig. 1 illustrates the working principle of FDM 3D printers. During the printing process, the printhead heats the filament to a molten state, and the molten material is precisely extruded to the printing platform through a preset path to complete the 3D solid construction with the help of a layer-by-layer stacking process.[35-38] After FDM manufacturing is complete, support materials can be easily removed by mechanical or chemical means.[39,40]

The nozzle structure characteristics of 3D printers affect

the filament stability and printing accuracy of filament, and Fig. 2 shows the common nozzle structures.[41,42] The main parameters of nozzle structure include liquefier diameter (D), liquefier length ($L_1$), nozzle length ($L_2$), outlet length ($L_3$), nozzle angle (β), and d.[23,30] From this, it can be analyzed that D directly affects the melt flow and pressure distribution in the nozzle, while $L_2$ and $L_3$ together control the melt uniformity and extrusion stability, except that the melt in the $L_1$ section is relatively stable, and its structure has less influence on the extrusion state of the melt, whereas D and $L_2$ have an effect on the magnitude of β. Based on the above conclusions, this paper focuses on the effects of D, $L_2$, and $L_3$ on the consumable extrusion stability and printing accuracy, and the rest of the parameters are determined to be 40 mm for $L_1$, and 3 mm for D. Moreover, we ensure that β is not greater than 90° after comprehensive consideration.[31,43,44]

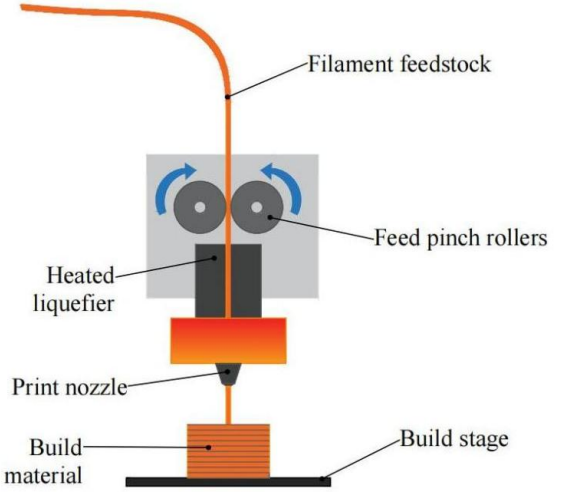


**Fig. 1:** FDM 3D printer working principle diagram.

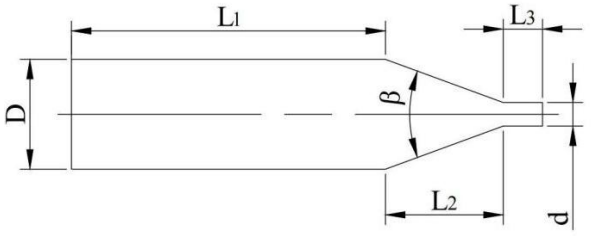


**Fig. 2:** Nozzle structure.

### 2.2 Orthogonal design

In order to efficiently investigate the effect of nozzle structure on the melt flow characteristics of PLA materials, a three-factor, three-level orthogonal experiment was designed to reduce the number of experiments and improve the experimental efficiency (Tables 1 and 2). The orthogonal experiments considered the key parameters of the nozzle structure, including D, $L_2$, and $L_3$, to systematically evaluate the effects of these parameters on the results of melt outlet viscosity, velocity, temperature and pressure distribution in the flow channel.

**Table 1:** Orthogonal experiment factor levels.

| Group | D/(mm) | $L_2$/(mm) | $L_3$/(mm) |
|---|---|---|---|
| 1 | 13 | 20 | 5 |
| 2 | 14 | 25 | 6 |
| 3 | 15 | 30 | 7 |

**Table 2:** Orthogonal array.

| Experiment Number | D/(mm) | $L_2$/(mm) | $L_3$/(mm) |
|---|---|---|---|
| 1 | 13 | 20 | 5 |
| 2 | 13 | 25 | 6 |
| 3 | 13 | 30 | 7 |
| 4 | 14 | 20 | 6 |
| 5 | 14 | 25 | 7 |
| 6 | 14 | 30 | 5 |
| 7 | 15 | 20 | 7 |
| 8 | 15 | 25 | 5 |
| 9 | 15 | 30 | 6 |

## 3. Simulation analysis

### 3.1 Simulation model

To analyze the fluid flow characteristics inside the nozzle, it is necessary to simulate and analyze the fluid inside the nozzle. The 3D model (Fig. 3a) is imported into the ANSYS-Workbench, and the mesh division of the fluid model is performed using the Polyflow numerical simulation module. An expansion layer is set for the outer wall of the fluid, the number of expansion layers is 5, the maximum thickness is set to 0.5 mm, and the multi-area method is selected to generate the mesh model (Fig. 3b).

### 3.2 Mathematical model

In the fluid simulation and computational analysis, considering the properties of polymer and the conditions of stable extrusion process, the following assumptions are made to simplify the modeling and analytical process:

1. The melt is regarded as an incompressible, non-Newtonian fluid;
2. Due to the overall heating of the mold, the flow field is a stable isothermal flow field;
3. The Reynolds number is much lower than in 2000, which indicates that the flow is laminar;
4. As the inertial force and gravity are much smaller than the viscous force, which can be ignored;
5. Plastic melt in the flow channel is completely filled and no slip phenomenon occurs.

In addition, the melt obeys the laws of conservation of mass, momentum, and energy during the flow process. These assumptions and laws provide the basis for theoretical analysis and calculations by Eqs.(1)-(3).[45-47]

$$\frac{\partial \rho}{\partial t}+\frac{\partial(\rho u_x)}{\partial x}+\frac{\partial(\rho u_y)}{\partial y}+\frac{\partial(\rho u_z)}{\partial z}=0 \quad (1)$$

$$\frac{\partial \rho}{\partial t}+\frac{\partial(\rho u_x)}{\partial x}+\frac{\partial(\rho u_y)}{\partial y}+\frac{\partial(\rho u_z)}{\partial z}=0 \quad (2)$$

$$\Sigma F=\rho q_V(\beta_2 v_2-\beta_1 v_1) \quad (3)$$

where ρ is the density; t is the time; $u_x$, $u_y$, $u_z$ is the velocity components of the fluid along the x, y and z directions. z is the position head; $\frac{\rho}{\rho g}$ is the pressure head; $\frac{v^2}{2g}$ is the velocity head. ΣF is the vector sum of all the external forces acting on the studied fluid plasma system; ρ is the density of the fluid; qv is the flow rate of the fluid; v is the velocity of the fluid; β is the momentum correction coefficient.

### 3.3 Material properties

#### 3.3.1 Boundary condition setting

The nozzle model designed in this experiment has a d of 3 mm and an $L_1$ of 40 mm and is printed with high-precision layering at 5 mm/s and a thickness of 1 mm. The corresponding flow rate was calculated according to Eq. (4), and it was set as the inlet motion boundary condition; the fluid surface was set as no-slip on the outer wall surface, the fluid velocity on the outer wall surface was kept the same as the wall velocity (the relative velocity was 0), and at the outlet boundary, it was a free-flow outflow.

$$Q=v_s\frac{\pi D^2}{4} \quad (4)$$

where Q is the volumetric flow rate; $v_s$ is the wire feed rate; D is the inlet diameter.

The recommended printing temperature range for PLA is 190 °C-230 °C.[48] In the actual 3D printing process, the printhead temperature was set at 190 °C-240 °C, considering the material properties, environmental factors, and subtle variations during the printing process. The proper temperature range (190 °C-240 °C) allows for good interaction between the PLA molecular chains, which helps to improve the coherence of the 3D printheads, and also ensures that the PLA material is sufficiently fused to form a denser structure when cooled down, thus guaranteeing the mechanical strength of the printed products.[49] Therefore, the inlet temperature is set to room temperature 293.15 K, and the wall temperature is 473.15 K. The specific boundary conditions are shown in Table 3.

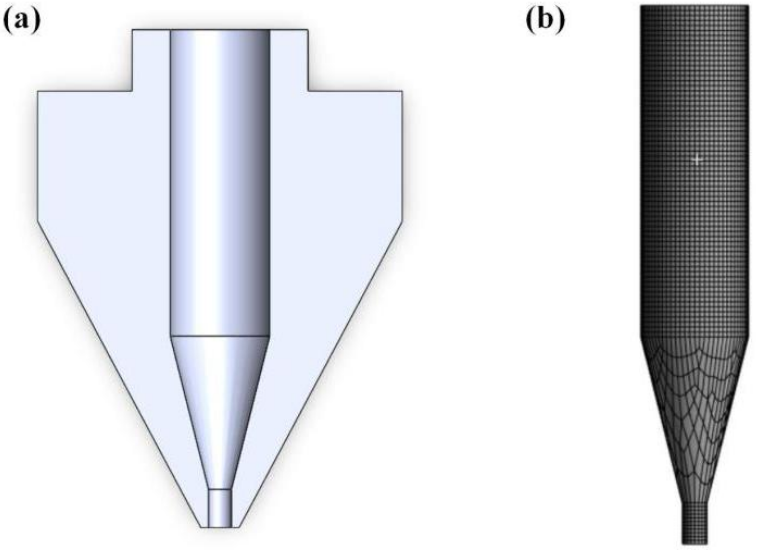


**Fig. 3:** (a) Diagram of the nozzle model;(b) Diagram of the nozzle grid.

**Table 3:** Basic parameters of boundary conditions.

| Boundary conditions | Boundary name | Boundary conditions |
|---|---|---|
| Flow boundary conditions | Inlet | Inflow |
| | Outlet | Outflow |
| | Wall | Zero wall velocity (vn=vs=0) |
| Thermal boundary conditions | Inlet | Temperature imposed (293.15 K) |
| | Outlet | Outflow |
| | Wall | Temperature imposed (473.15 K) |

### 3.3.2 Simulation Parameters

In this paper, the Bird-Carreau model is used to describe the variation rule of melt viscosity with shear rate, as shown in Eq. (5).[49,50] In addition, in order to further consider the effect of temperature, the viscosity-temperature correction model of Approximate Arrhenius law (Eq. (6)) is introduced to correct the temperature of PLA's constitutive equation, and the specific parameters of the equation are shown in Tables 4 and 5.[51]

$$H\left(\dot{\gamma}\right) = \eta_\infty + (\eta_0 - \eta_\infty)\left[1 + \left(\lambda\dot{\gamma}\right)^2\right]^{\frac{n-1}{2}} \quad (5)$$

$$h(T) = \exp[-\alpha(T - T_\alpha)] \quad (6)$$

where $\eta_\infty$ is the infinite shear viscosity; $\eta_0$ is the zero shear viscosity; $\lambda$ is the relaxation time; n is the non-Newtonian exponent; $\dot{\gamma}$ is the shear rate; $\alpha$ is the temperature coefficient; $T_\alpha$ is the reference temperature.

## 4. Simulation results and discussion

### 4.1 Analysis of simulation results

The orthogonal simulation model of nozzle flow channel was constructed based on Polyflow, and 9 groups of experimental data were obtained in Table 6. In the 3D printing process, the melt exit parameters directly determine the print quality: the outlet velocity characterizes the stability of the extrusion flow, which affects the print size accuracy; the outlet pressure reflects the melt flow resistance, which is a key indicator for judging the risk of nozzle clogging; and the outlet viscosity embodies the material rheological state, which directly affects the surface quality of the filament. However, changes in shear rate can alter the viscosity of the melt. Meanwhile, the temperature distribution of the melt in the runner will also affect the stability of the nozzle discharge. Based on this, in the post-processing analysis of the experimental results, the focus is on the temperature distribution, velocity, pressure, shear rate, and viscosity in the nozzle channel. The results of orthogonal experiments show that the temperature field, pressure field, velocity field and shear rate distribution states of the melt flow channel in different simulation groups are

**Table 4:** Basic parameters of boundary conditions.[52]

| Rheological parameters | $\eta_\infty$(Pa·s) | $\eta_0$(Pa·s) | $\lambda$ | n | $\alpha$ | $T_\alpha$(K) |
|---|---|---|---|---|---|---|
| Value | 0 | 1000 | 1 | 0.4 | 0.0025 | 463.15 |

**Table 5:** Basic parameters of PLA properties.[53]

| Basic parameters | Poisson's ratio | Density (kg/m³) | Melting point (°C) | Specific heat capacity [J/(kg·K)] | Thermal conductivity [W/(m·K)] | Viscosity (Pa·s) |
|---|---|---|---|---|---|---|
| Value | 0.35 | 1250 | 190~230 | 2040 | 0.231 | 1200 |

**Table 6:** Simulation results of orthogonal experiment.

| Experiment Number | Levels and Values of (Technological) Factors | | |
|---|---|---|---|
| | Velocity, v/(mm/s) | Pressure, P/(Pa) | Viscosity, η/(Pa·s) |
| 1 | 95.2741 | 579.5050 | 47.6783 |
| 2 | 95.2742 | 676.0510 | 47.6835 |
| 3 | 95.2743 | 716.4140 | 47.6874 |
| 4 | 110.5060 | 727.7060 | 43.6244 |
| 5 | 110.5070 | 764.9910 | 43.6278 |
| 6 | 110.4990 | 593.8940 | 43.7977 |
| 7 | 126.8880 | 811.7240 | 40.1555 |
| 8 | 126.8880 | 649.9250 | 40.1479 |
| 9 | 126.8770 | 751.6100 | 40.2437 |

similar. Therefore, the following analysis takes test 1 as a typical working condition for detailed analysis and illustration.

### 4.1.1 Flow channel temperature

By analyzing the melt flow channel temperature field of nine sets of simulation tests Fig. 4, the results show a sharp temperature increase, rising from 295.9 K at the inlet to 472.2 K before stabilizing at 473.1 K. As seen in Fig. 4a, the wall temperature rises significantly faster than the center due to direct contact with the heating wall, while the incoming material (295.9 K) establishes a thermal gradient. This efficient heating process not only shortens the material's residence time in the nozzle but also prevents print defects caused by uneven melting. Thus, the well-designed structure of the melting zone and nozzle inlet plays a crucial role in enhancing print quality and efficiency.

### 4.1.2 Velocity

Analyzing Figs. 5(a, c-k), the melt velocity varies significantly at the junction of nozzle throat and outlet zone, while it is relatively stable in the liquefier zone and nozzle throat. At the junction of nozzle throat and outlet zone, due to the reduction of flow channel diameter, the melt is compressed, and the velocity increases significantly and reaches the maximum value in the outlet zone. This phenomenon is closely related to the change of channel geometry, the reduction of flow channel diameter leads to the acceleration of melt velocity, while the wall friction is enhanced, which further aggravates the inhomogeneity of velocity distribution.

Combined with Fig. 5b for further analysis, the melt outlet velocity in the liquefier zone is relatively stable, maintained at about 5.00 mm/s; while in the nozzle throat, the velocity starts to rise gradually, and the velocity in the outlet zone rises significantly to 95.27 mm/s. The melt outlet velocity in the nozzle outlet surface shows the distribution of high in the center and low in the surroundings. The main reason for this phenomenon is that the flow path in the center area is short and direct, and the melt is easy to flow out, so the velocity is higher, while the edge area is lower due to the longer flow path and the influence of wall friction. In addition, the melt temperature in the heating section is high and uniformly distributed, with good fluidity and relatively stable velocity distribution.

### 4.1.3 Pressure

Analyzing Fig. 6, the melt channel pressure gradually decreases along the outlet direction. Combined with specific data, the pressure in the liquefier zone gradually decreases from 156.5 KPa to 140.9 KPa (10% decrease); while from the nozzle throat to the liquefier zone, the pressure significantly decreases from 138.3 KPa to 0.6 KPa (99.6% decrease) and stabilizes at 0.6 KPa at the exit surface. This phenomenon is is dominated by two factors: (1) the melt in the flow process of viscous friction leads to energy dissipation, which is manifested as a gradual decrease of pressure along the exit direction. Especially at the junction of nozzle throat and outlet

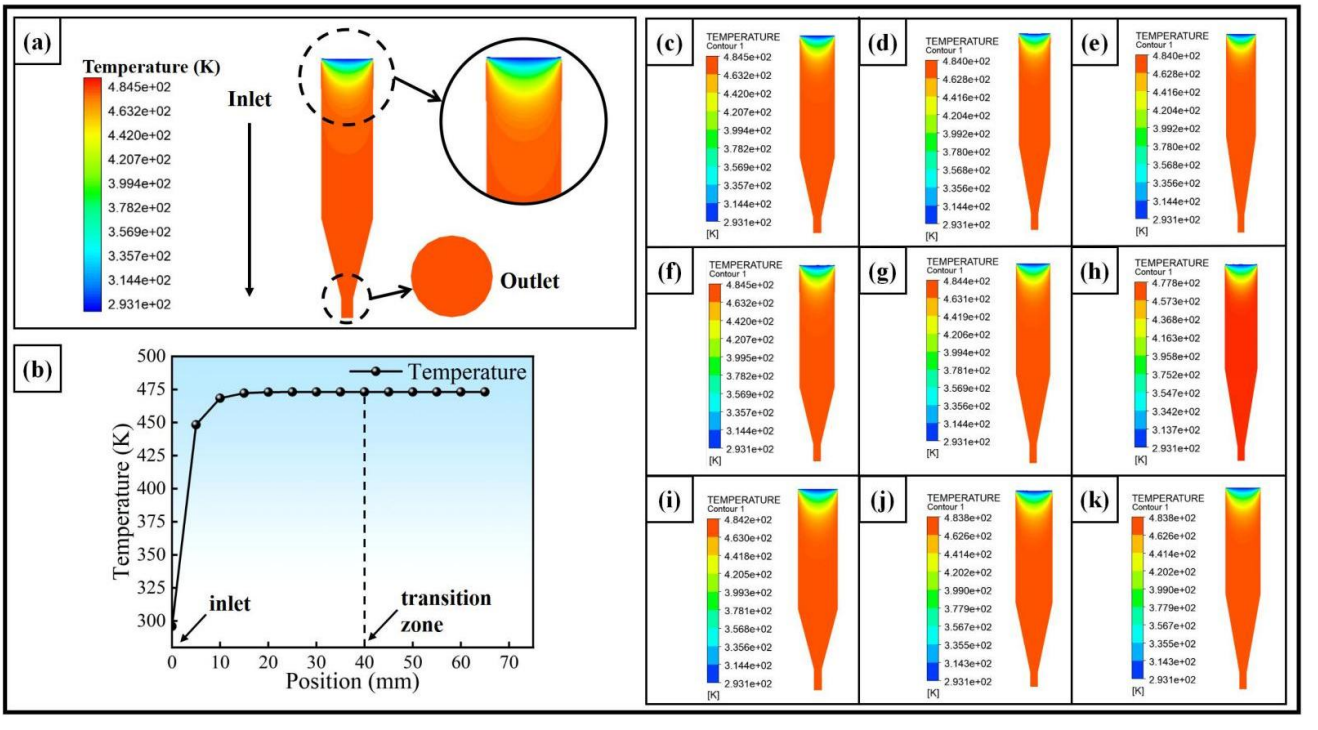


**Fig. 4:** (a) Flow channel temperature and outlet temperature; (b) Line graph of temperature distribution along the outlet direction in the flow channel; (c-k) Temperature simulation result.

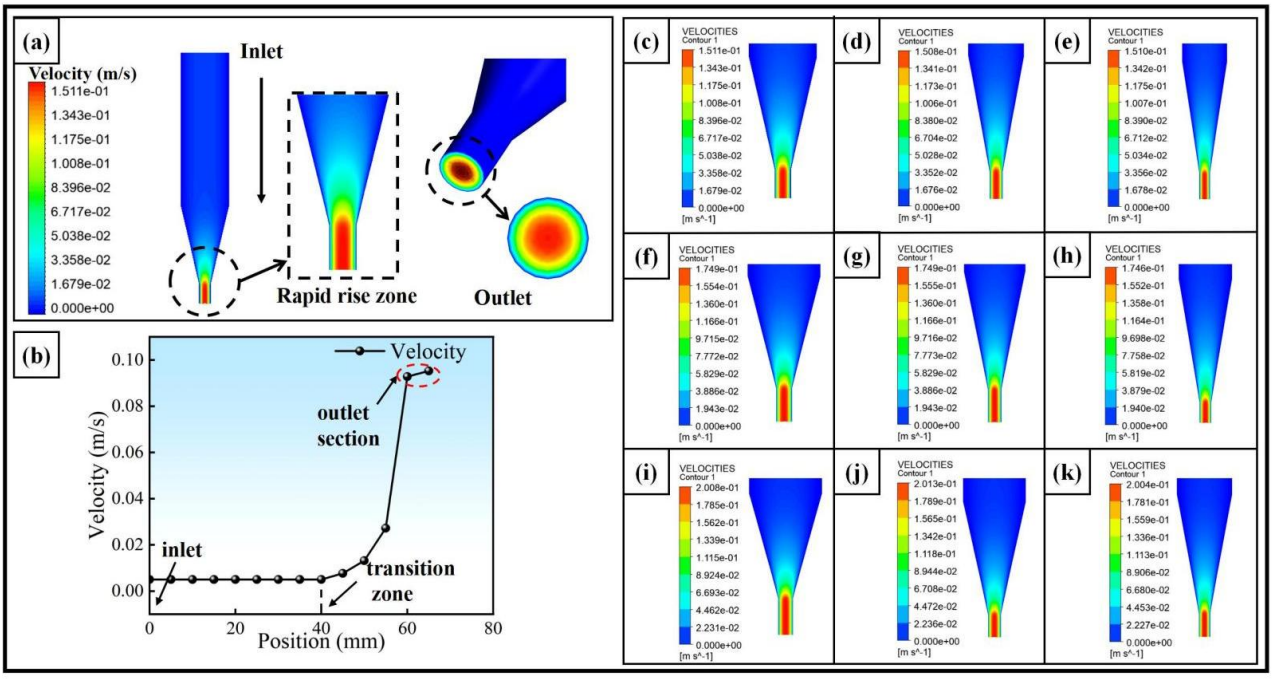


**Fig. 5:** (a) Velocity in the flow channel versus outlet velocity; (b) Line graph of velocity distribution in the flow channel along the outlet direction; (c-k) Full velocity simulation results.

zone, due to the significant changes in the size of the flow channel, the flow resistance increases sharply, and the pressure loss is further increased. (2) From the aforementioned melt flow rate, when the material enters the nozzle throat, the melt flow rate begins to rise gradually. From Bernoulli Eq. (7), it can be seen that in the ideal fluid, the pressure decreases when the flow rate increases, while in the actual fluid, viscosity and friction will lead to pressure loss, consume mechanical energy and reduce the pressure, additional energy is needed to compensate for the flow. Therefore, an increase in flow velocity leads to a decrease in static pressure.

$$P_1 + \frac{1}{2}\rho v_1^2 = P_2 + \frac{1}{2}\rho v_2^2 + \triangle P_{loss} \quad (7)$$

where P is the static pressure of the fluid, ρ is the density of the fluid, v is the velocity of the fluid, $\triangle P_{loss}$ is the pressure loss due to viscous resistance.

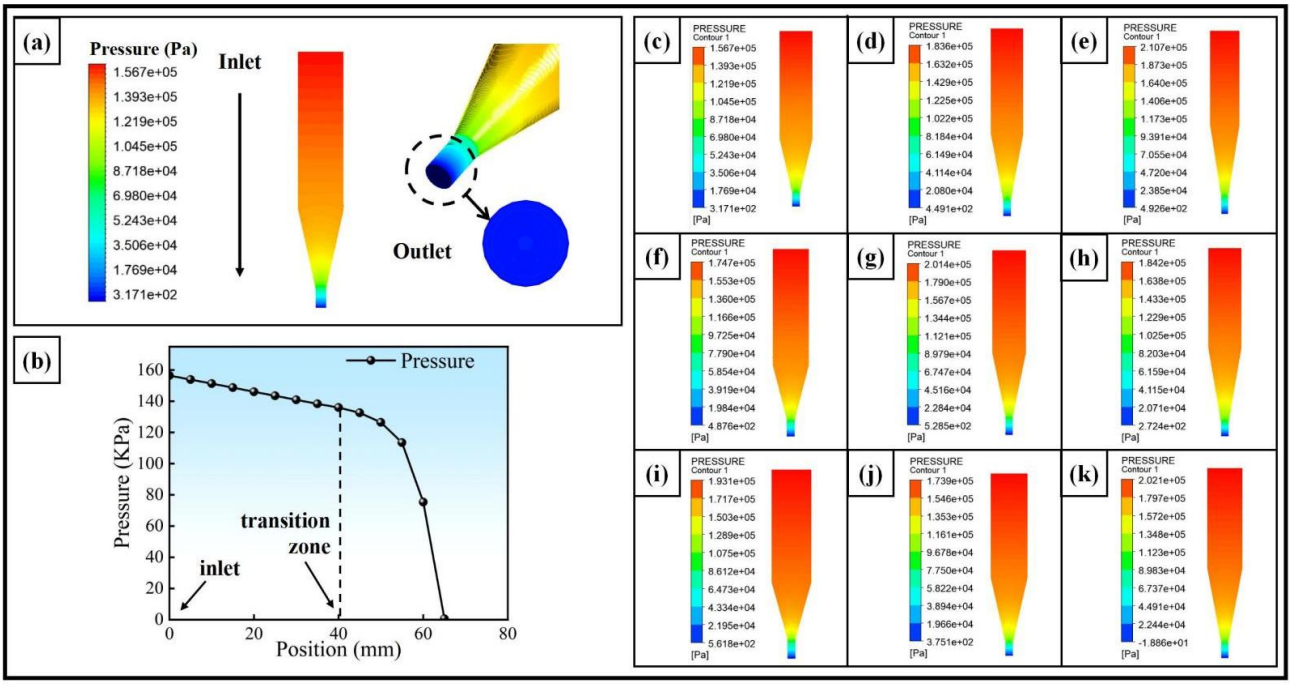


**Fig. 6:** (a) Flow channel pressure and outlet pressure; (b) Line graph of pressure distribution in the flow channel along the outlet direction; (c-k) All pressure simulation results.

#### 4.1.4 Shear rate and viscosity

Analyzing Figs. 7(a, c-k), the melt shear rate in the nozzle outlet surface presents a low center region, high wall, and in the liquefier zone and nozzle throat junction rises significantly. This phenomenon is caused by the synergistic effect of two aspects: (1) the melt by frictional resistance, the center layer of flow velocity is higher than the wall, and the center layer velocity gradient is lower than the wall layer velocity gradient, resulting in an increase in shear rate; (2) flow channel mutation triggered by the concentration of local shear stresses, the role of the fluid on the embodiment of the shear rate increases.

The further analysis of Fig. 7b shows that the shear rate is stable in the liquefier zone, maintaining at 1.953-1.974 $s^{-1}$, while in the nozzle throat, it gradually increases to 30.24 $s^{-1}$, and in the outlet zone, the shear rate is significantly elevated to 139.1-159.5 $s^{-1}$. The shear rate of the melt exit is characterized by a low center and high wall distribution. The melt outlet shear rate on the nozzle outlet surface exhibits a distribution characteristic that is low at the center and high at the wall. This is mainly due to the smooth flow of the melt in the center region, while the rapid increase of the flow rate with the narrowing of the flow channel leads to enhanced friction near the wall and increased shear, which is manifested by a further increase in the shear rate.

Meanwhile, from the analysis of the viscosity data in Fig. 7b, it can be observed that as the material is transported forward (liquefier zone-nozzle throat-outlet zone), the viscosity of the material decreases significantly from 624 Pa·s to 47 Pa·s, with a decrease of about 92.4%. This phenomenon is closely related to the structural evolution of PLA molecular chains under high shear conditions. As the shear rate increases, PLA molecular chains gradually transform from disordered packing to oriented arrangement along the flow direction, which reduces the entanglement density of molecular chains in the melt and significantly decreases the internal friction during flow. Meanwhile, high-speed shear inhibits the ordered packing and crystalline growth of molecular chains, further lowering the viscous resistance of the melt. These synergistic changes in microstructure collectively contribute to the significant shear-thinning behavior of the PLA melt.

The experimental results show that the nine designed nozzle structures can achieve a stable temperature distribution inside the nozzle, reaching 473 K at the nozzle outlet surface. The changes in nozzle structure have varying degrees of impact on fluid velocity, pressure, and shear rate within the flow channel. Among them, the temperature rises rapidly to 473.15 K in the liquefier zone and remains stable. The melt velocity increases sharply in the nozzle throat, forming a characteristic distribution of fast in the center and slow at the edge. The pressure decreases continuously along the flow direction, and a significant pressure drop occurs at the junction of the nozzle throat and outlet zone. The shear rate gradually

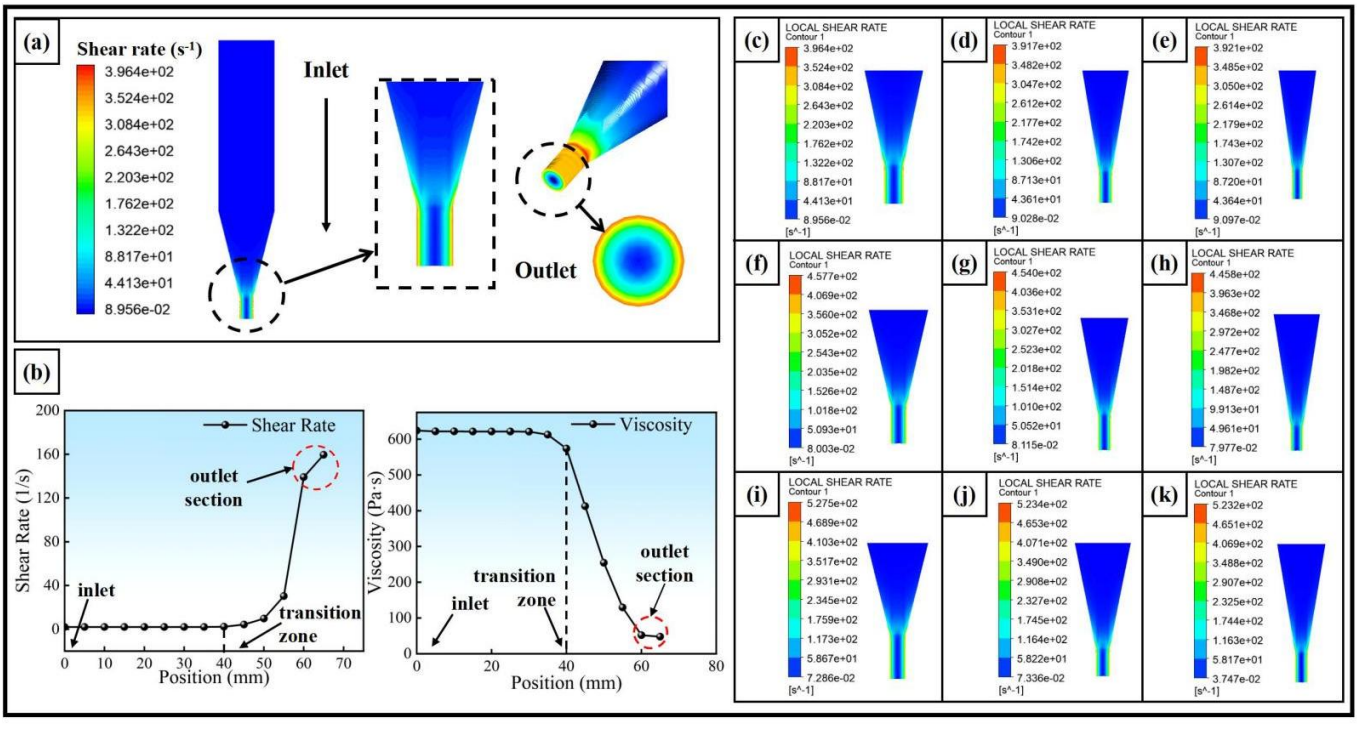


**Fig. 7:** (a) Flow channel shear rate and outlet shear rate; (b) Line graphs of shear rate distribution along the outlet direction in the flow channel and viscosity distribution along the outlet direction in the flow channel; (c-k) All shear rate simulation results.

direction, and a significant pressure drop occurs at the junction of the nozzle throat and outlet zone. The shear rate gradually increases along the flow direction, and the near-wall zone is significantly higher than the center zone, and this distribution leads to obvious shear thinning effect. Therefore, based on this, the subsequent optimization will focus on examining the influence of nozzle structure on the melt outlet velocity, pressure loss and shear rate, and improve the comprehensive performance of the nozzle by balancing the relationship between the three.

### 4.2 Range analysis method

The range analysis method was used to process the data in this study in order to ascertain the extent to which each element affected the melt state in the nozzle and to thoroughly examine the data in Table 6 The following formula was used to get the mean (Eqs.(8) and (9)) and extreme deviation:

$$\overline{K_{ij}} = \frac{K_{ij}}{s} \tag{8}$$

$$R_j = \max\overline{K_{ij}} - \min\overline{K_{ij}} \tag{9}$$

where $K_{ij}$ is the number of levels of each component in the orthogonal experiment, $\overline{K_{ij}}$ is the extreme deviation of the factor in the j column, s is the average of the test results under the identical conditions, and $R_j$ is the sum of all test results when the j factor takes the i level.

#### 4.2.1 Outlet velocity

Fig. 8 shows the table of range analysis of outlet velocity range and the effect of each factor on the outlet rate obtained from the simulation results. The analysis of outlet velocity shows that as D increases from 13 mm to 15 mm, the outlet velocity shows a significant increasing trend from 95.2742 mm/s to 126.8843 mm/s, which is an increase of 33.2%. The results of the range analysis show that the range value of D is as high as 31.6101, which far exceeds the effects of $L_2$ (0.0063) and $L_3$ (0.0041), indicating that D is the key factor in determining the outlet velocity. This phenomenon is due to the fact that under the condition of constant inlet velocity, according to the law of conservation of mass, the increase of D leads to a significant increase in the melt flow rate Q ($Q \propto D^2$) through the nozzle, and in order to maintain the mass balance, the outlet sectional velocity is bound to increase accordingly. At the same time, the larger D reduces the flow resistance, which is conducive to the melt obtaining higher kinetic energy in the outlet zone, resulting in a more stable extrusion process.

(a)

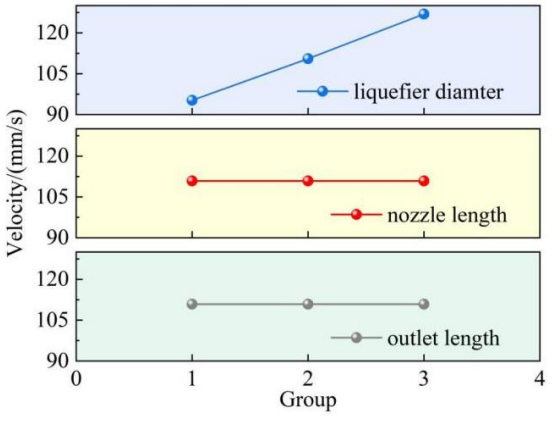


(b)

| Group | D | $L_2$ | $L_3$ |
|---|---|---|---|
| 1 | 95.2742 | 110.8894 | 110.8870 |
| 2 | 110.5040 | 110.8897 | 110.8857 |
| 3 | 126.8843 | 110.8834 | 110.8898 |
| Range $R_j$ | 31.6101 | 0.0063 | 0.0041 |
| Optimal Case | 3 | 2 | 3 |
| Order of Influence | 1 | 2 | 3 |

**Fig. 8:** (a) Results of the analysis of the range analysis of the export velocity; (b) Graph of the velocity change.

(a)

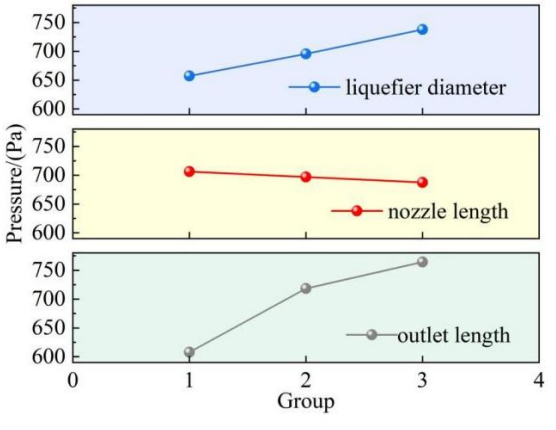


(b)

| Group | D | $L_2$ | $L_3$ |
|---|---|---|---|
| 1 | 657.3233 | 706.3117 | 607.7747 |
| 2 | 695.5303 | 696.9890 | 718.4557 |
| 3 | 737.7530 | 687.3060 | 764.3763 |
| Range $R_j$ | 80.4297 | 19.0057 | 156.6016 |
| Optimal Case | 3 | 1 | 3 |
| Order of Influence | 2 | 3 | 1 |

**Fig. 9:** (a) Results of outlet pressure range analysis; (b) Pressure variation profile.

#### 4.2.2 Outlet pressure

Combining the table of range analysis of the range value of outlet pressure and the effect of each factor on the outlet pressure obtained from the simulation results (Fig. 9), it was found that when $L_3$ was increased from 5 mm to 7 mm, the outlet pressure increased from 607.7747 Pa to 764.3763 Pa, which is an increase of about 25.8%. Comparing the degree of influence of each parameter by range analysis, the range value of $L_3$ is 156.6016, which has the most significant influence on the nozzle performance, followed by D (80.4297) and $L_2$ (19.0057). This pressure change rule can be explained by the Bernoulli Eqs. (8) and (9): the increase of $L_3$ extends the melt flow path, so that the viscous resistance effect is enhanced, to overcome the increased flow resistance and to maintain the energy balance of the system, the outlet pressure must be increased accordingly. In addition, the longer outlet zone also enhances the shear history of the melt, further affecting the pressure distribution characteristics.

#### 4.2.3 Viscosity

The range analysis table of the range value of outlet viscosity and the effect of each factor on outlet viscosity obtained from the simulation results are shown in Fig. 10. The experimental data show that as D increases from 13 mm to 15 mm, the melt outlet viscosity shows a significant decreasing trend, specifically from 47.6831 Pa·s to 40.1824 Pa·s, with a decrease of 15.7%. It was found by a range analysis that the range value of D was as high as 7.5007, which significantly exceeded the effects of $L_2$ (0.0902) and $L_3$ (0.0509). This phenomenon can be explained by rheological theory: an increase in D leads to an increase in flow Q ($Q \propto D^2$), and although the overall shear rate decreases, the outlet zone produces a localized high shear rate due to the constriction of the flow channel. According to the shear thinning effect of the Bird-Carreau model, the final manifestation is a decrease in viscosity with increasing D.

### 4.3 Optimum structure

#### 4.3.1 Principle of genetic algorithm

To optimize the structural parameters of the 3 mm large-bore nozzle, this study adopts GA for multi-objective optimization. Relying on the principle of survival of the fittest in the process of biological evolution, the GA aims to realize the gradual approximation of the objective function to a better solution in the optimization problem. Through the three basic operations of selection, crossover and mutation, the initial population is iteratively updated to gradually screen out individuals with higher fitness. After many iterations, the optimal solution that satisfies the requirements of the fitness function is finally found. GA shows significant advantages in solving complex optimization problems with their unique evolutionary mechanism and powerful global search capability.[54]

#### 4.3.2 Build the fitness function

The construction of a fitness function is central in the optimization framework of the GA, which is inspired by the law in nature that species fitness determines the chance of reproduction. In this algorithm, fitness is a key metric for assessing how close an individual is to the optimal solution and its potential contribution. A higher value of fitness indicates a more optimal solution for that individual. In this experiment, outlet velocity, pressure and viscosity are used as the optimization objectives. Based on the principle of least squares, polynomial fitting was performed on nine sets of orthogonal experiment data using MATLAB. To improve the fitting accuracy of the regression equation, the highest order term of the equation was extended to three times. Eventually, three regression Eqs. (10)-(12) with velocity (V), Pressure (P),

(a)

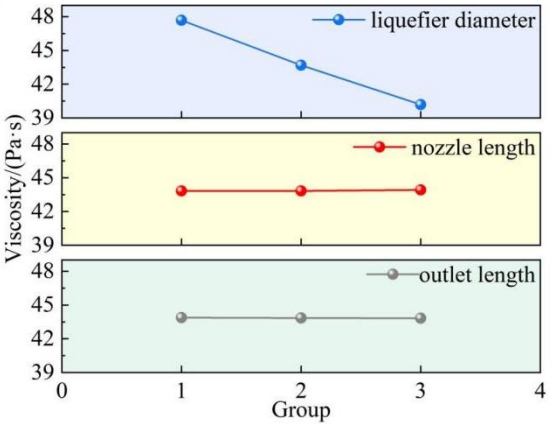


(b)

| Group | D | $L_2$ | $L_3$ |
|---|---|---|---|
| 1 | 47.6831 | 43.8194 | 43.8746 |
| 2 | 43.6833 | 43.8197 | 43.8505 |
| 3 | 40.1824 | 43.9096 | 43.8237 |
| Range $R_j$ | 7.5007 | 0.0902 | 0.0509 |
| Optimal Case | 1 | 3 | 1 |
| Order of Influence | 1 | 2 | 3 |

**Fig. 10:** (a) Results of outlet viscosity range analysis; (b) Viscosity variation profile.

$$V = 0.5643D^2 - 0.0004L_2^2 + 0.0020D^3 - 0.0003L_2^3 - 0.0031D^2L_2 - 0.0007D^2L_3 - 0.0001L_2^2L_3 + 0.0017DL_2^2 + 0.0006L^2L_3^2 \quad (10)$$

$$P = -9.5486D^2 + 4.1426L_2^2 - 7.7710D^3 + 1.1732L_2^3 + 12.4825D^2L_2 + 4.0959D^2L_3 + 0.8602L_2^2L_3 - 7.1196DL_2^2 - 4.2535L_2L_3^2 \quad (11)$$

$$\eta = 1.3853D^2 - 0.1152L_2^2 + 0.3143D^3 - 0.0590L_2^3 - 0.5974D^2L_2 - 0.1336D^2L_3 - 0.0118L_2^2L_3 + 0.3350DL_2^2 + 0.1099L_2L_3^2 \quad (12)$$

and viscosity (η) as independent variables were obtained, respectively, and were used as fitness functions in the GA for subsequent optimization calculations.

#### 4.3.3 Build the objective function

To optimize the nozzle performance, the vector expression of the independent variable optimization model was constructed as shown in Eq. (13). Where the optimized independent variables include D, $L_2$, and $L_3$, represented as $x_1$, $x_2$ and $x_3$, respectively.

$$x = [D, L_2, L_3]^T = [x_1, x_2, x_3]^T \quad (13)$$

Additionally, the regression equations for the viscosity of the fluid, outlet velocity, and outlet pressure are represented as $y_1(x), y_2(x)$ and $y_3(x)$. The goal of optimization is to reduce the viscosity of the fluid in the flow channel while increasing the outlet velocity and outlet pressure. Equation 14 illustrates the construction of the optimization objective function.

$$\min f(x) = [-y_1(x), -y_2(x), y_3(x)]^T \quad (14)$$

#### 4.3.4 Constraint condition

According to the range of values of orthogonal experiment parameters, boundary constraints are imposed on independent variables and as shown in Eq. (15). Together, these constraints constitute the boundary constraints of the independent variables, as shown in Eqs. (16)-(18), to ensure that the values of the parameters in the optimization process are within a reasonable range.

$$h_1(x_1) = \begin{cases} x_1 - Dmax \le 0 \\ Dmax - x_1 \le 0 \end{cases} \quad (15)$$

$$h_2(x_2) = \begin{cases} x_2 - Pmax \le 0 \\ Pmax - x_2 \le 0 \end{cases} \quad (16)$$

$$h_3(x_3) = \begin{cases} x_3 - \eta max \le 0 \\ \eta max - x_3 \le 0 \end{cases} \quad (17)$$

$$h(x) = [h_1(x), h_2(x), h_3(x)]^T \quad (18)$$

#### 4.3.5 Optimal model simulation

Based on the principle of GA, using MATLAB combined with the fitness function and nozzle basic conditions to write a program, the optimal solution conclusion: D is 15, $L_2$ is 23.587, $L_3$ is 6.980. Combined with the optimal conclusion to design the simulation test table again, as shown in Table 7.

**Table 7:** Simulation results of orthogonal experiment.

| Experiment Number | D/(mm) | $L_2$/(mm) | $L_3$/(mm) |
|---|---|---|---|
| 1 | 15 | 23.587 | 6.980 |
| 2 | 15 | 23.000 | 7.000 |
| 3 | 15 | 24.000 | 7.000 |

#### 4.3.6 Optimization results

Based on the test scheme in Table 7, the 3D printing nozzle model was simulated using Polyflow, and the simulation results are shown in Fig. 11 and Table 8. The analysis results show that when D is 15 mm, $L_2$ is 23-24 mm, and $L_3$ is 7 mm, the outlet velocity of the melt at the nozzle outlet reaches 126.889 mm/s, and the outlet pressure is increased to 806.141-809.434 Pa, while the viscosity is reduced to 40.1553-40.1556 Pa·s. This ensures that the melt in the extrusion process has good mobility during the extrusion process, which significantly improves the printing accuracy and ensures the smoothness of the printing process. The optimization results show that this parameter combination is highly reliable and effective.

**Table 8:** Optimized results.

| Experiment Number | Levels and Values of (Technological) Factors | | |
|---|---|---|---|
| | Velocity, v/(mm/s) | Pressure, P/(Pa) | Viscosity, η/(Pa·s) |
| 1 | 126.8890 | 806.1410 | 40.1553 |
| 2 | 126.8890 | 808.5820 | 40.1555 |
| 3 | 126.8890 | 809.4340 | 40.1556 |

Compared with the results of the nine sets of tests before optimization, the present set of tests showed significant combined advantages in terms of outlet velocity, pressure and viscosity. The larger D reduces the flow resistance and increases the melt flow rate and pressure; the moderate $L_2$ optimizes the flow path and avoids energy loss; and the reasonable $L_3$ ensures the uniformity of melt flow. This group of tests significantly improved the nozzle performance by optimizing the parameter combination, which verified the validity of the optimization results.

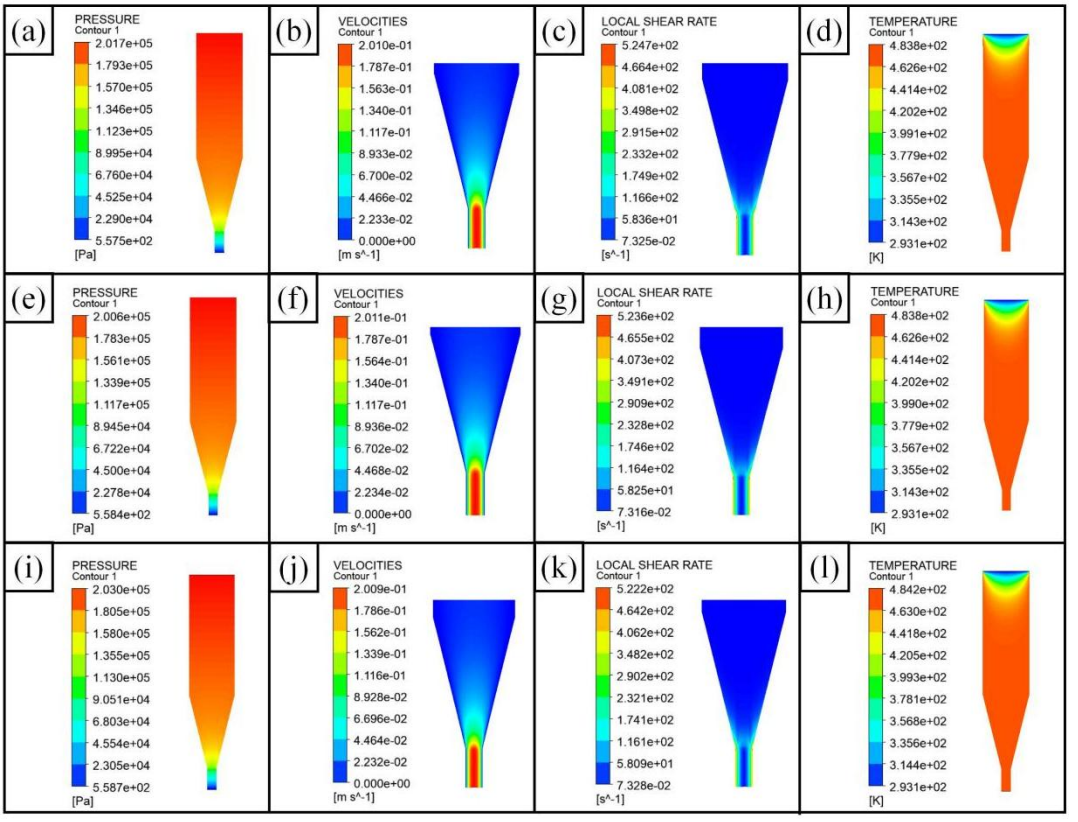


**Fig. 11:** (a-d): Cloud diagram for the outcome of optimization test 1; (e-h): Cloud diagram for the outcome of optimization test 2; (i-l): Cloud diagram for the outcome of optimization test 3.

## 5. Conclusion

In this study, the influence of nozzle structural parameters on the melt flow process is systematically investigated by combining numerical simulation and optimal design for the problem of melt flow characteristics in large-bore FDM 3D printing nozzles. Through establishing a numerical model of the nozzle with d of 3 mm and using ANSYS Polyflow to carry out three-factor and three-level orthogonal simulation experiments, we focus on analyzing the effects of three key structural parameters, namely D, $L_2$ and $L_3$, on the melt flow characteristics of the PLA melt. The following conclusions were obtained:

1. Orthogonal tests using Polyflow reveal the distribution of temperature, pressure, velocity and shear rate fields inside the nozzle. The simulation results show that the temperature inside the nozzle rises rapidly to 473.15 K in the liquefier zone and remains stable. The melt velocity increases sharply in the nozzle throat, forming a characteristic distribution of fast at the center and slow at the edge. The pressure decreases continuously along the flow direction, and a significant pressure drop occurs at the junction of the nozzle throat and outlet zone. The shear rate gradually increases along the flow direction, and the near-wall zone is significantly higher than the center zone, and this distribution leads to obvious shear thinning phenomenon.

2. Range analysis quantified how each structural parameter influenced the melt flow state, showing that D most significantly affected outlet velocity with a 99.9% contribution rate, increasing D from 13 mm to 15 mm while adjusting $L_2$ from 20 mm to 25 mm and $L_3$ from 5 mm to 7 mm boosted velocity by 33.2%. For pressure distribution, $L_3$ plays a dominant role as it increases from 5 mm to 7 mm, which together with the increase in D by 2 mm increases the pressure by 25.8%, while the increase in $L_2$ decreases the outlet pressure. Regarding viscosity, all parameters exerted measurable effects with sensitivity following $D > L_2 > L_3$, where enlarging D and $L_2$ increased viscosity while shortening $L_3$ decreased it. These results demonstrate D's primary control velocity, $L_3$ 's governing influence on pressure, and all three parameters' combined yet differentiated impacts on melt viscosity.

3. The conclusions of the above studies show that the design of the nozzle flow channel structure has a significant role in regulating the melt extrusion stability. Accordingly, in this study, GA was used to carry out a multi-objective optimization solution for the nozzle structure, and a polynomial regression model was established by least-squares fitting with outlet velocity, outlet pressure and viscosity as

optimization objectives. The optimal combinations of nozzle structure parameters are determined as D = 15 mm, $L_2$ = 23-24 mm, and $L_3$ = 7 mm, and the optimized nozzle structure has strong comprehensive performance, which can effectively improve the process performance of large-diameter FDM printing.

**Acknowledgements**

This work is supported by the Basic Public Welfare Research Programme of Zhejiang Province (grant number: LTGS23E030001), Science and Technology Research Project of Quzhou City (grant number: 2023K211, 2024K054, 2024K148), Science and Technology Innovation Activity Programme for College Students in Zhejiang Province (grant number: 2024R434A002).

**Conflict of Interest**

There is no conflict of interest.

**Supporting Information**

Not applicable.

**References**

[1] T. Tezel, V. Kovan, E. S. Topal, Effects of the printing parameters on short-term creep behaviors of three-dimensional printed polymers, *Journal of Applied Polymer Science*, 2019, **136**, 47564, doi: 10.1002/app.47564.

[2] J. Gopinathan, I. Noh, Recent trends in bioinks for 3D printing, *Biomaterials Research*, 2018, **22**, 11, doi: 10.1186/s40824-018-0122-1.

[3] N. Shahrubudin, T. C. Lee, R. Ramlan, An overview on 3D printing technology: technological, materials, and applications, *Procedia Manufacturing*, 2019, **35**, 1286-1296, doi: 10.1016/j.promfg.2019.06.089.

[4] P. Dudek, FDM 3D printing technology in manufacturing composite elements, *Archives of Metallurgy and Materials*, 2013, **58**, 1415-1418, doi: 10.2478/amm-2013-0186.

[5] C. Yang, X. Tian, D. Li, Y. Cao, F. Zhao, C. Shi, Influence of thermal processing conditions in 3D printing on the crystallinity and mechanical properties of PEEK material, *Journal of Materials Processing Technology*, 2017, **248**, 1-7, doi: 10.1016/j.jmatprotec.2017.04.027.

[6] T. N. Tran, I. S. Bayer, J. A. Heredia-Guerrero, M. Frugone, M. Lagomarsino, F. Maggio, A. Athanassiou, Cocoa shell waste biofilaments for 3D printing applications, *Macromolecular Materials and Engineering*, 2017, **302**, 1700219, doi: 10.1002/mame.201700219.

[7] M. Lei, Q. Wei, M. Li, J. Zhang, R. Yang, Y. Wang, Numerical simulation and experimental study the effects of process parameters on filament morphology and mechanical properties of FDM 3D printed PLA/GNPs nanocomposite, *Polymers*, 2022, **14**, 3081, doi: 10.3390/polym14153081.

[8] N. T. Tuli, S. Khatun, A. Bin Rashid, Unlocking the future of precision manufacturing: a comprehensive exploration of 3D printing with fiber-reinforced composites in aerospace, automotive, medical, and consumer industries, *Heliyon*, 2024, **10**, e27328, doi: 10.1016/j.heliyon.2024.e27328.

[9] M. S. Karkun, S. Dharmalinga, 3D printing technology in aerospace industry–a review, *International Journal of Aviation, Aeronautics, and Aerospace*, 2022, **9**, 4, doi: 10.15394/ijaaa.2022.1708

[10] I. Buj-Corral, A. Tejo-Otero, F. Fenollosa-Artés, Use of FDM technology in healthcare applications: recent advances, *Fused Deposition Modeling Based 3D Printing*, Cham: Springer International Publishing, 2021, 277-297, doi: 10.1007/978-3-030-68024-4_15.

[11] S. Pessoa, A. S. Guimarães, S. S. Lucas, N. Simões, 3D printing in the construction industry - A systematic review of the thermal performance in buildings, *Renewable and Sustainable Energy Reviews*, 2021, **141**, 110794, doi: 10.1016/j.rser.2021.110794.

[12] J. L. Saorin, M. D. Diaz-Alemán, J. De la Torre-Cantero, C. Meier, I. Pérez Conesa, Design and validation of an open source 3D printer based on digital ultraviolet light processing (DLP), for the improvement of traditional artistic casting techniques for microsculptures, *Applied Sciences*, 2021, **11**, 3197, doi: 10.3390/app11073197.

[13] M. K. Niaki, S. Ali Torabi, F. Nonino, Why manufacturers adopt additive manufacturing technologies: The role of sustainability, *Journal of Cleaner Production*, 2019, **222**, 381-392, doi: 10.1016/j.jclepro.2019.03.019.

[14] C. Ge, L. Priyadarshini, D. Cormier, L. Pan, J. Tuber, A preliminary study of cushion properties of a 3D printed thermoplastic polyurethane Kelvin foam, *Packaging Technology and Science*, 2018, **31**, 361-368, doi: 10.1002/pts.2330.

[15] U. Scheithauer, E. Schwarzer, H.-J. Richter, T. Moritz, Thermoplastic 3D printing: an additive manufacturing method for producing dense ceramics, *International Journal of Applied Ceramic Technology*, 2015, **12**, 26-31, doi: 10.1111/ijac.12306.

[16] U. Scheithauer, T. Slawik, E. Schwarzer, H.-J. Richter, T. Moritz, A. Michaelis, Additive manufacturing of metal-ceramic-composites by thermoplastic 3D-printing (3DTP), *Journal of Ceramic Science and Technology*, 2015, doi: 10.4416/JCST2014-00045.

[17] A. Manoj, R. C. Panda, Biodegradable filament for 3D printing process: a review, *Engineered Science*, 2022, **18**, 11-19, doi: 10.30919/es8d616.

[18] J. Liu, L. Sun, W. Xu, Q. Wang, S. Yu, J. Sun, Current

advances and future perspectives of 3D printing natural-derived biopolymers, *Carbohydrate Polymers*, 2019, **207**, 297-316, doi: 10.1016/j.carbpol.2018.11.077.

[19] J. Sedlak, Z. Joska, J. Jansky, J. Zouhar, S. Kolomy, M. Slany, A. Svasta, J. Jirousek, Analysis of the mechanical properties of 3D-printed plastic samples subjected to selected degradation effects, *Materials*, 2023, **16**, 3268, doi: 10.3390/ma16083268.

[20] S. Maurya, B. Malik, P. Sharma, A. Singh, R. Chalisgaonkar, Investigation of different parameters of cube printed using PLA by FDM 3D printer, *Materials Today*: *Proceedings*, 2022, **64**, 1217-1222, doi: 10.1016/j.matpr.2022.03.700.

[21] A. P. Valerga, M. Batista, J. Salguero, F. Girot, Influence of PLA filament conditions on characteristics of FDM parts, *Materials*, 2018, **11**, 1322, doi: 10.3390/ma11081322.

[22] B. G. Thiam, A. El Magri, H. R. Vanaei, S. Vaudreuil, 3D printed and conventional membranes: a review, *Polymers*, 2022, **14**, 1023, doi: 10.3390/polym14051023.

[23] B. N. Turner, R. Strong, S. A. Gold, A review of melt extrusion additive manufacturing processes: I. Process design and modeling, *Rapid Prototyping Journal*, 2014, **20**, 192-204, doi: 10.1108/rpj-01-2013-0012.

[24] T. Tezel, V. Kovan, Determination of optimum production parameters for 3D printers based on nozzle diameter, *Rapid Prototyping Journal*, 2022, **28**, 185-194, doi: 10.1108/rpj-08-2020-0185.

[25] C. Chukwudozie, B. Bourdin, K. Yoshioka, A variational phase-field model for hydraulic fracturing in porous media, *Computer Methods in Applied Mechanics and Engineering*, 2019, **347**, 957-982, doi: 10.1016/j.cma.2018.12.037.

[26] S. L. Messimer, A. E. Patterson, N. Muna, A. P. Deshpande, T. Rocha Pereira, Characterization and processing behavior of heated aluminum-polycarbonate composite build plates for the FDM additive manufacturing process, *Journal of Manufacturing and Materials Processing*, 2018, **2**, 12, doi: 10.3390/jmmp2010012.

[27] M. Hikmat, S. Rostam, Y. M. Ahmed, Investigation of tensile property-based Taguchi method of PLA parts fabricated by FDM 3D printing technology, *Results in Engineering*, 2021, **11**, 100264, doi: 10.1016/j.rineng.2021.100264.

[28] B. Singh, R. Kumar, J. Singh Chohan, Multi-objective optimization of 3D Printing process using genetic algorithm for fabrication of copper reinforced ABS parts, *Materials Today*: *Proceedings*, 2022, **48**, 981-988, doi: 10.1016/j.matpr.2021.06.264.

[29] D. Fischer, C. Eßbach, R. Schönherr, D. Dietrich, D. Nickel, Improving inner structure and properties of additive manufactured amorphous plastic parts: The effects of extrusion nozzle diameter and layer height, *Additive Manufacturing*, 2022, **51**, 102596, doi: 10.1016/j.addma.2022.102596.

[30] O. Hıra, S. Yücedağ, S. Samankan, Ö. Y. Çiçek, A. Altınkaynak, Numerical and experimental analysis of optimal nozzle dimensions for FDM printers, *Progress in Additive Manufacturing*, 2022, **7**, 823-838, doi: 10.1007/s40964-021-00241-y.

[31] Y. Yu, G. Zhang, Q. Xiao, A. Ji, Y. Feng, G. Zhu, L. Zhou, 3D printer nozzle structure form optimal structural analysis, *Processes*, 2024, **12**, 1482, doi: 10.3390/pr12071482.

[32] X. Zhang, X. Huang, B. Liu, S. Chen, Study on the melt rheological characterization of micro-tube gas-assisted extrusion based on the cross-scale viscoelastic model, *Polymers*, 2024, **16**, 973, doi: 10.3390/polym16070973.

[33] Z. Xu, R. Sun, W. Lu, S. Patil, J. Mays, K. S. Schweizer, S. Cheng, Nature of steady-state fast flow in entangled polymer melts: chain stretching, shear thinning, and viscosity scaling, *Macromolecules*, 2022, **55**, 10737-10750, doi: 10.1021/acs.macromol.2c01345.

[34] B. Xu, Theoretical and experimental approach of the viscosity of polymer melt under micro-scale effect, *Journal of Mechanical Engineering*, 2010, **46**, 125, doi: 10.3901/jme.2010.19.125.

[35] H. Xia, J. Lu, G. Tryggvason, A numerical study of the effect of viscoelastic stresses in fused filament fabrication, *Computer Methods in Applied Mechanics and Engineering*, 2019, **346**, 242-259, doi: 10.1016/j.cma.2018.11.031.

[36] K. E. Aslani, D. Chaidas, J. Kechagias, P. Kyratsis, K. Salonitis, Quality performance evaluation of thin walled PLA 3D printed parts using the taguchi method and grey relational analysis, *Journal of Manufacturing and Materials Processing*, 2020, **4**, 47, doi: 10.3390/jmmp4020047.

[37] A. Alafaghani, A. Qattawi, Investigating the effect of fused deposition modeling processing parameters using Taguchi design of experiment method, *Journal of Manufacturing Processes*, 2018, **36**, 164-174, doi: 10.1016/j.jmapro.2018.09.025.

[38] S. Wickramasinghe, T. Do, P. Tran, FDM-based 3D printing of polymer and associated composite: a review on mechanical properties, defects and treatments, *Polymers*, 2020, **12**, 1529, doi: 10.3390/polym12071529.

[39] F. Ning, W. Cong, J. Qiu, J. Wei, S. Wang, Additive manufacturing of carbon fiber reinforced thermoplastic composites using fused deposition modeling, *Composites Part B*: *Engineering*, 2015, **80**, 369-378, doi: 10.1016/j.compositesb.2015.06.013.

[40] X. Wang, Z. Liu, H. Wang, C. Zeng, Direct 3D printing of piezoelectrets: process feasibility, prototypes fabrication and device performance, *Engineered Science*, 2022, **21**, 800, doi: 10.30919/es8d800

[41] H. S. Ramanath, C. K. Chua, K. F. Leong, K. D. Shah, Melt flow behaviour of poly-ε-caprolactone in fused deposition

modelling, *Journal of Materials Science*: *Materials in Medicine*, 2008, **19**, 2541-2550, doi: 10.1007/s10856-007-3203-6.
[42] N. Mostafa, H. M. Syed, S. Igor, G. Andrew, A study of melt flow analysis of an ABS-iron composite in fused deposition modelling process, *Tsinghua Science & Technology*, 2009, **14**, 29-37, doi: 10.1016/S1007-0214(09)70063-X.
[43] Q. Gao, M. Zhou, L. Zhu, X. Duan, Flow field analysis and structure optimization of FDM 3D printer nozzle, *Modular Machine Tool & Automatic Manufacturing Technique*, 2018, **11**, 34-47, doi: 10.13462/j.cnki.mmtamt.2018.11.010.
[44] J. Z. Liang, J. N. Ness, Effect of die angle on flow behaviour for high impact polystyrene melt, *Polymer Testing*, 1997, **16**, 403-412, doi: 10.1016/S0142-9418(97)00001-9.
[45] T. Oyinloye, W. Yoon, Application of computational fluid dynamics (CFD) simulation for the effective design of food 3D printing (a review), *Processes*, 2021, **9**, 1867, doi: 10.3390/pr9111867.
[46] T. Norton, D. Sun, Computational fluid dynamics (CFD)–an effective and efficient design and analysis tool for the food industry: a review, *Trends in Food Science & Technology*, 2006, **17**, 600-620, doi: 10.1016/j.tifs.2006.05.004.
[47] T. Norton, D. Sun, J. Grant, R. Fallon, V. Dodd, Applications of computational fluid dynamics (CFD) in the modelling and design of ventilation systems in the agricultural industry: a review, *Bioresource Technology*, 2007, **98**, 2386-2414, doi: 10.1016/j.biortech.2006.11.025.
[48] S. Lee, J. W. Wee, Effect of temperature and relative humidity on hydrolytic degradation of additively manufactured PLA: Characterization and artificial neural network modeling, *Polymer Degradation and Stability*, 2024, **230**, 111055, doi: 10.1016/j.polymdegradstab.2024.111055.
[49] Q. Mo, S. Zhang, T. Chen, W. Cao, Fit and Evaluate the Viscous Models Used for ABS, *Key Engineering Materials*, 2022, **905**, 231-237, doi: 10.4028/www.scientific.net/KEM.905.231.
[50] T. M. Oyinloye, W. B. Yoon, Stability of 3D printing using a mixture of pea protein and alginate: Precision and application of additive layer manufacturing simulation approach for stress distribution, *Journal of Food Engineering*, 2021, **288**, 110127, doi: 10.1016/j.jfoodeng.2020.110127.
[51] W. Tang, Y. Liu, H. Zhang, C. Wang, New approximate formula for Arrhenius temperature integral, *Thermochimica Acta*, 2003, **408**, 39-43, doi: 10.1016/S0040-6031(03)00310-1.
[52] Z. Yulian, L. Xin, A. Qi, H. Zhigang, Numerical simulation of meshing co-rotating twin screw extrusion process under non-isothermal conditions, *Food and Machinery*, 2019, 35: 76-79, doi: 10.13652/j.issn.1003-5788.2019.04.015.
[53] S. Zhou, X. Zhang, Collaborative Optimization of Wire Feeding Mechanism and Nozzle for 3D Printer, *Machine Tool & Hydraulics*, 2023, **51**, 27-33, doi: 10.13785/j.cnki.nmggydxxbzrkxb.2022.04.013.
[54] S. Katoch, S. S. Chauhan, V. Kumar, A review on genetic algorithm: past, present, and future, *Multimedia Tools and Applications*, 2021, **80**, 8091-8126, doi: 10.1007/s11042-020-10139-6.